Supporting Information

Tensile properties of single- and multi-type mixed fibre bundles of spider silk

Siripanyo Promnil[1, *], Daniele Liprandi[1], Tom Illing[1,2], Maitry Jani[1], Paula Heinz[1], Jonas O. Wolff[1]

[1]Evolutionary Biomechanics, Zoological Institute and Museum, University of Greifswald, Loitzer Str. 26, 17489 Greifswald, Germany.
[2]Institute of Physics, University of Greifswald, Felix-Hausdorff-Str. 6, 17489 Greifswald, Germany.

*_Corresponding email:_ siripanyo.promnil@uni-greifswald.de

On the statistical analysis of the fracture mechanics of silk bundles of *P. phalangioides*

The studied silk bundles show a scattering of strength values which can be investigated using classic mechanical analysis. For fibrous material, it is supposed that the failure derives from the weakest chain link present in the fibre. When this is true, the strength of the material during repeated measurements follows a two-parameter Weibull distribution[1, 2]:

$$P(\sigma) = 1 - \exp\left(- S \cdot \left(\frac{\sigma}{\sigma_0}\right)^m \right) \tag{1}$$

Where $P(\sigma)$ is an increasing function bounded from 0 to 1 that expresses the probability of a fibre to fail for a stress value of σ, and S is a geometrical parameter. The two parameters are the shape parameter m and the scale parameter σ_0. The value of the shape parameter m indicates how repeatable is the strength of the fibre, i.e. if the considered material shows a wider (larger values) or thicker (lower values) scattering of their strength values. The geometrical parameter S scales with the length, cross-section, or volume of the fibre, depending on the effective defect proportionality of the fibre, and on the dimensionality of the dissipated energy during fracture[3, 4]. In literature, while all densities have been analysed, a predominance of length-dependent defect density studies are found, including for polymeric fibres[4-6]. To better represent this proportionality, often a Modified Weibull distribution, or double-humped Weibull distribution, is used

$$P(\sigma) = 1 - \exp\left(- \left(\frac{A}{A_0}\right)^v \cdot \left(\frac{\sigma}{\sigma_0}\right)^m \right) \tag{2}$$

Where, again, A can indicate the length, cross-sectional area, or volume of the fibre, and A_0 is its reference value, often assumed equal to a unitary value, as its independent from the other parameters and it is only needed to render G dimensionless[2-9]. When the parameter v is equal to 1, Equation (2) becomes of the same form as Equation (1). When $v = 0$, the geometrical dependency disappears. The introduction of the parameter v is needed to compensate for the non-Weibull geometrical effects[3, 6]. In a study conducted on spider silk data, v was intended as the fractal dimension of the fracture energy dissipation[7].

From Equation (2), it is immediate to derive that, according to Weibull's theory, there is a defined relationship between the ratios of strengths and the ratios of the size of the fibres:

$$\log\left(\frac{\sigma_1}{\sigma_2}\right) = -\frac{v}{m}\log\left(\frac{S_1}{S_2}\right) \tag{3}$$

This relationship can be used to determine the value of v, provided that the value of m is already obtained using Equation (1).

To validate the agreement of our data with classical mechanics, we first applied Equation (1) to each bundle type separately. To do so, we have used both the linear regression method, and the maximum likelihood method, finding compatible results between the two. All bundles agree with Weibull's distribution, with the manually collected PMS bundles being the one with the weakest R^2 value, equal to $R^2 = 0.839$. We could then proceed to extract the values of the geometrical scaling v for each silk type, using the cross-sectional areas measured for

each of our bundle as our geometrical feature s. The results for *P. phalangioides* obtained through the linear regression method are shown in Table 1.

From the Weibull analysis presented in Table 1, and visualised in Figure 1, it can be seen how bridging lines are, at the same time, the most variable silk bundle, with a shape parameter of 2.39, and the ones with the highest characteristic strength, 1121.9 MPa. This result can be surprising when considering that bridging lines are formed by 2 fibres coming from the same silk gland. At the other end of this range, we find *P. phalangioides* gumfoot. Gumfoot bundles showed a low characteristic strength, but a higher repeatability than any other silk product. This mechanical difference correlates with the different production techniques of the two bundles: bridging lines are quickly spun by the spider with the help of its fourth pair of legs, leading to a possible generation of multiple defects along the length of the fibre. Gumfoot bundles, on the other end, are spun while slowly descending from an upper substrate to a lower substrate. This result indicates that the spinning speed, and not the number of fibres, may be responsible for a higher or lower defect density in this spider species.

Table 1 also presents the size effect parameter v. Our results show that four out of six bundles present a considerable size effect. The value of v for these four bundles, which are the three draglines and the bridging line, range from 1.89 to 4.92, a non-trivial result, as often in literature this value is assumed to be limited to the range between 0 and 1, as described in the previous section.

When $v > 1$, the material exhibits enhanced size effects beyond those predicted by classical linear elastic fracture mechanics. The scaling behaviour found here implies that the effective flaw size decreases more rapidly with specimen dimensions than geometric similarity would predict. This phenomenon has been documented in other biological materials, notably bamboo fibres, where Wang and Shao[8] reported similar deviations from classical Weibull scaling; we also found a more recent work, investigating sponge fibrous structure, where strength scaled inversely with the square of specimen dimension rather than the expected square root relationship, allegedly due to the inner structure of these materials[10]. To help us understand what this implies, we explore classic fracture mechanics, starting from the Griffith's criterion.

According to Griffith's criterion, the stress to reach fracture σ_f scales as $\sqrt{\frac{GE}{\pi a}}$, where γ is the strain energy release rate, E is the elastic modulus, and a is the characteristic flaw size[11-13]. For a linearly elastic cylindrical fibre, the equation can be rewritten as

$$\sigma_f = \sqrt{\frac{\gamma E}{D}} \tag{4}$$

where D is the fibre diameter. This formulation indicates that the stress should scale with the inverse square root of the diameter. We calculate the equivalent diameter of a bundle by using the straightforward geometrical relationship $d = 2\sqrt{\frac{A}{\pi}}$. The results of this analysis are reported in Table 2 and illustrated in Figure 3. Five of the six silk bundle types demonstrate statistically significant correlations between strength and the square root of the modulus-to-diameter ratio $\sqrt{E/d}$. The strength of these correlations varies across silk types, with bridging lines and walking draglines showing the strongest adherence to the energy criterion.

If we go back to Equation (3), and we consider the cross-section as the geometrical feature being considered, we obtain that, for a cylindrical fibre, the stress to fracture should scale with the known value

$$\sigma_2 = \sigma_1 \left(\frac{D_2}{D_1}\right)^{-\frac{2v}{m}} \tag{5}$$

which leads to the same value reported in the Equation (4) for a value of $\frac{v}{m} = \frac{1}{4}$. However, in our case, the values of this ration are much higher, as we discussed in the previous paragraph. The agreement of our data with both theories, and the disagreement with the quantitative comparison, are to be related to the presence of the Young's modulus in Equation (4); indeed, *P. phalangioides* produces fibre bundles which agree with classical fracture analysis, but also produces fibre bundle of the same type, and during the same behaviour, with different Young's modulus. This variation cannot be excluded, and cannot be represented just through an average. To better illustrate this, we have run the correlation $\sigma \propto 1/\sqrt{d}$, also reported in Table 2. The p-value and the R^2 both decrease for every silk bundle type excluding drop-down draglines made of 4 fibres.

These results indicate that, despite their nonlinear behaviour these silk bundles still show a relationship between the young's modulus and strength. Furthermore, it also shows that the variation of Young's moduli in a single bundle cannot be just reconducted to its own average, but instead, each bundle has to be considered individually. Spider silk is engineered to be able to achieve its performances by tuning not only its size and its fibre type, ie, the glands involved in the bundle production, but somehow also its stiffness during each single silk spinning.

In this scenario, the results found about mechanical properties of gumfoot bundles is particularly interesting. Their mechanical properties appear to not scale with the cross-sectional area. This could indicate that they are composed of a main load carrier, which has consistent diameter, while the other fibres in the bundle do not participate in the load transfer. This is in contrast with the SEM images we have obtained, where it appears that parallel fibres run from one end of the sample to the other. Another option would be that the cross-sectional area measurements are afflicted by a systematic error, due to the non-cylindrical fibres, or the presence of coatings, or other structures which affect the effective cross-sectional area of the bundle. To understand this phenomenon, we need to interrogate the internal mechanics of each bundle.
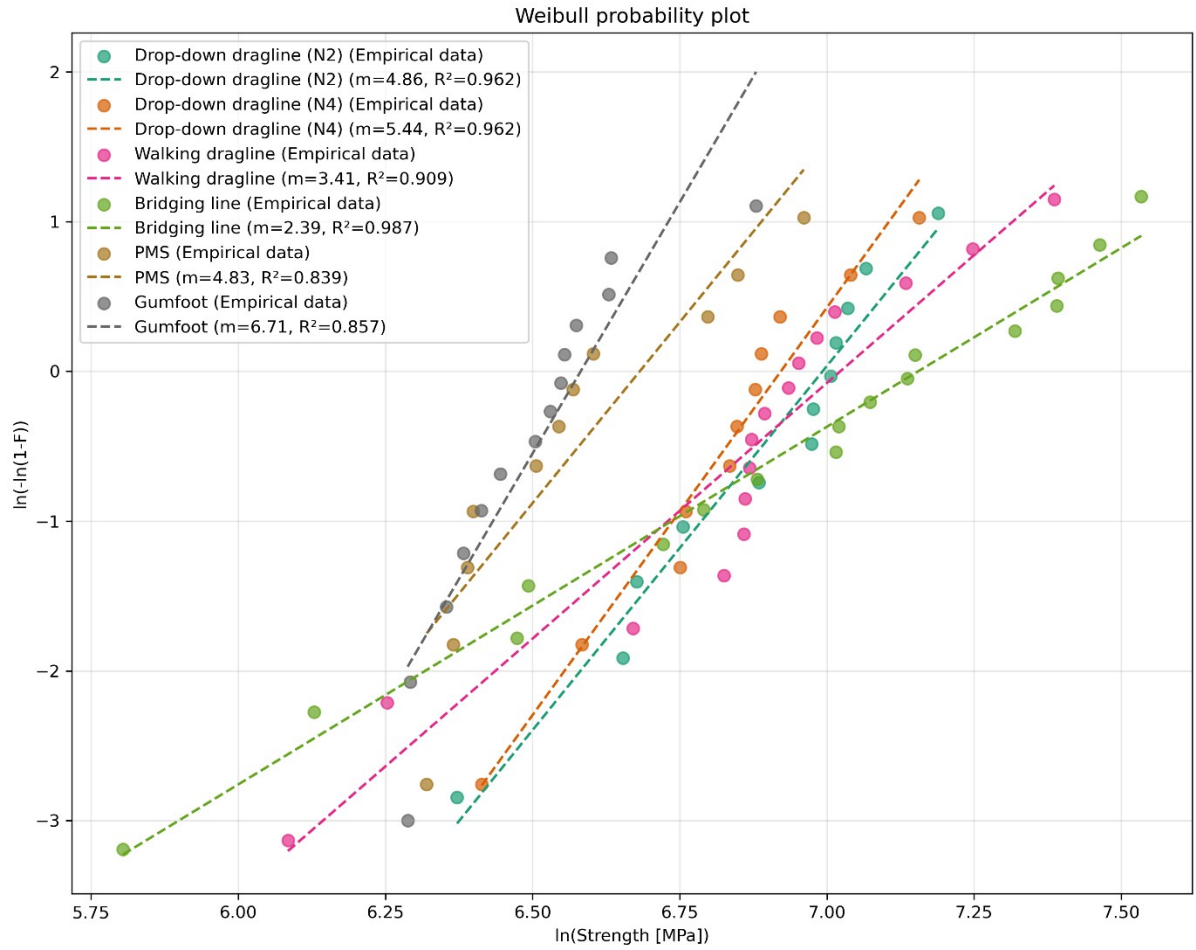
Figure S1 Weibull plot for *P. phalangioides*, with linear regression results reported as dashed lines for each silk bundle type. All bundle types agree with the weakest-chain link distribution.
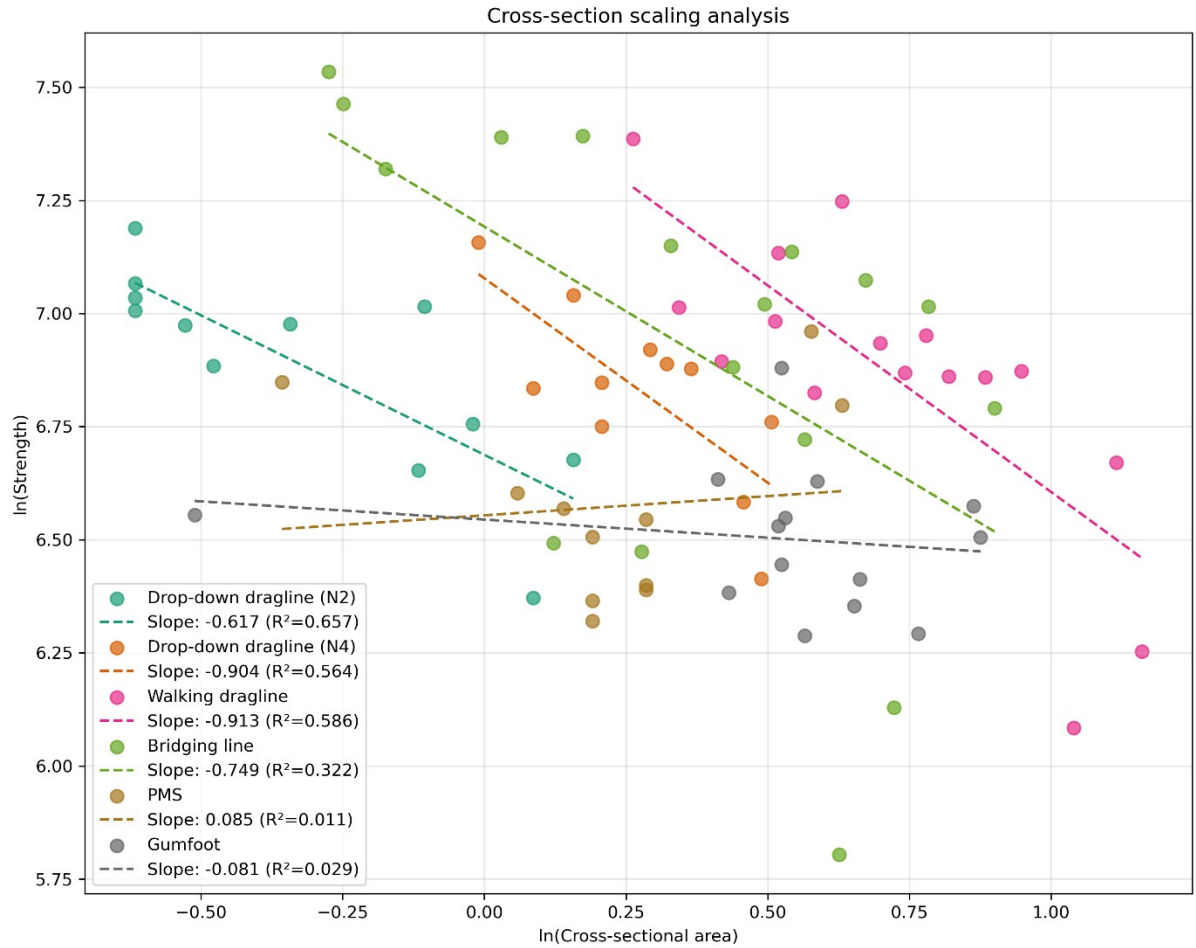
Figure S2 Correlation plot between the logarithm of the strength i.e. stress at break, and the logarithm of the cross-sectional area, for each measured bundle. Linear regression fits (dashed lines) are reported. Dragline bundles report a $R^2 > 0.5$ and a strong negative slope, which surpasses the prediction made by the Weibull distribution. PMS and gumfoot bundles show no correlation between the strength and the cross-sectional area.
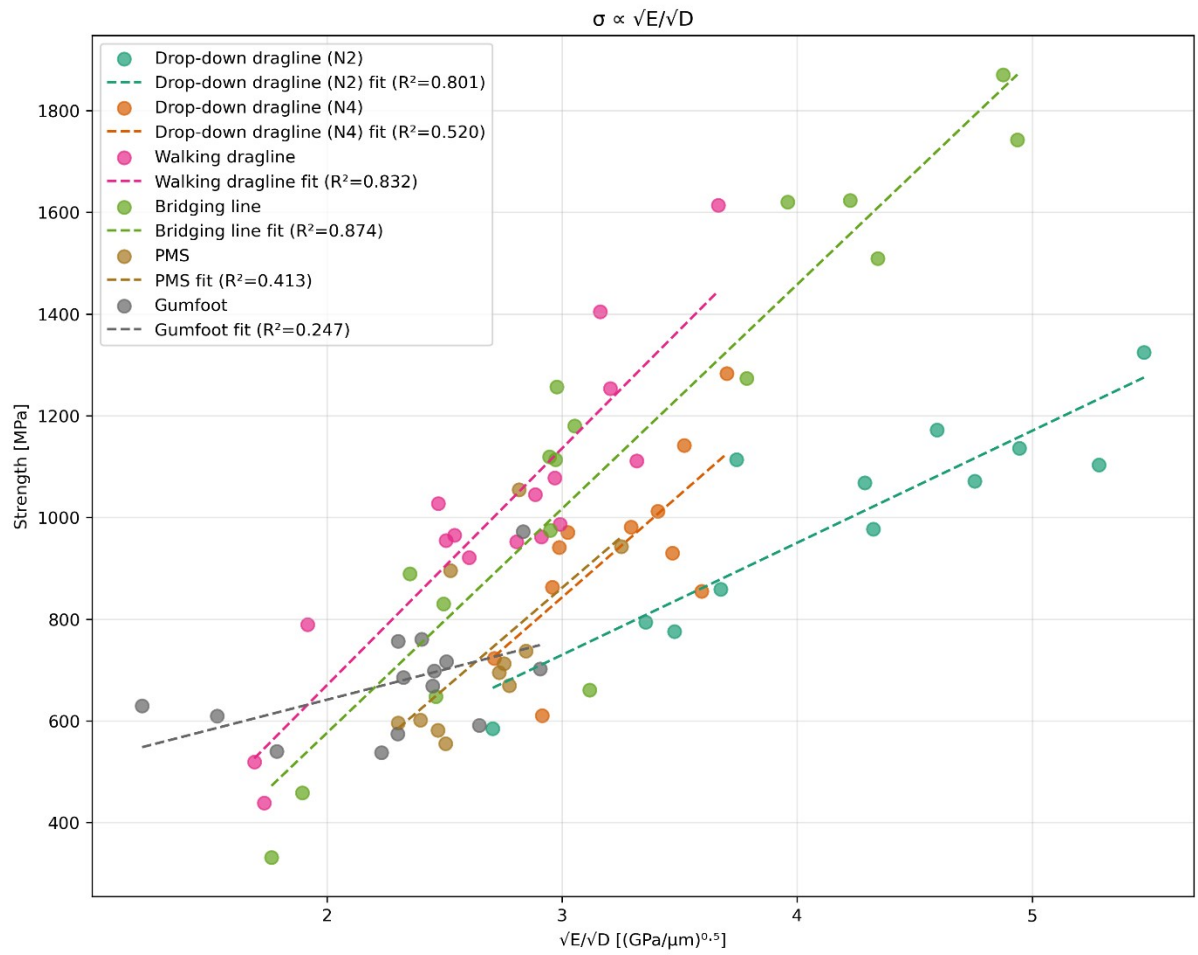
Figure S3 Fracture mechanics relationships for *P. phalangioides* silk bundles. The plots demonstrate the correlation between stress at break and the square root of the modulus-to-diameter ratio for each silk type. Linear regression fits (dashed lines) validate the prediction illustrated in [13] that strength scales with the square root of modulus divided by diameter, as predicted by Griffith's criterion.

Table S1 Results of the two-parameter Weibull analysis conducted on each silk type for *P. phalangioides*, and the scale parameter v found when studying the proportionality between strength and cross-section according to the modified Weibull distribution, with between brackets its significance.

Silk Type	Sample Size	σ [MPa]	$\Delta\sigma$ [MPa]	CV	m	σ_0 [MPa]	R²	v
Drop-down dragline (N2)	12	998.3	198.4	0.199	4.86	1088.6	0.962	2.999 (**)
Drop-down dragline (N4)	11	937.4	174.6	0.186	5.44	1014.2	0.962	4.92 (**)
Walking dragline	16	1001.4	277.2	0.277	3.41	1121.9	0.909	3.117 (**)
Bridging line	17	1123.7	440.8	0.392	2.39	1280.4	0.987	1.789 (**)
PMS	11	731	156.7	0.214	4.83	798	0.839	-0.41 (ns)
Gumfoot	14	674.6	108.8	0.161	6.71	721.8	0.857	0.54 (ns)

Table S2 Fracture mechanics analysis correlating bundle equivalent diameter with tensile strength for *P. phalangioides*, using the relationships $\sigma \propto \sqrt{E}/\sqrt{d}$ and $\sigma \propto 1/\sqrt{d}$ for each silk bundle type, presenting coefficients of determination (r²), statistical significance (p values).

Silk Type	d [μm]	E [GPa]	σ vs $\sqrt{E/d}$ p-value	σ vs $\sqrt{E/d}$ R²	σ vs $\sqrt{1/d}$ p-value	σ vs $\sqrt{1/d}$ R²
Drop-down dragline (N2)	0.973	17.098	8.41E-05	0.801	0.001	0.670
Drop-down dragline (N4)	1.302	13.575	0.012	0.520	0.006	0.586
Walking dragline	1.628	11.907	8.72E-07	0.832	4.17E-04	0.601
Bridging line	1.366	14.281	3.93E-08	0.874	0.003	0.462
PMS	1.272	9.035	0.033	0.413	0.810	0.007
Gumfoot	1.487	7.860	0.071	0.247	0.626	0.020

On the bundle properties of *N. cellanus*

We repeated the analysis using the mechanical data of the four bundle types we collected for *N. cellanus*. Due to the lack of variety in bundle cross-sectional areas, the lower sample size, and the lower number of bundle types produced by the spider, it was not possible to extract the same amount of significant information for *N. cellanus*, compared to *P. phalangioides*. However, Table 3 and Figure 4 shows that the bundles follow Weibull's theory, and thus agree with the weakest link principle. Gumfoot bundles of *N. cellanus* also present a low shape parameter when compared with the ones of *P. phalangioides*, while drop-down draglines show higher reproducibility.

Furthermore, it is interesting to observe, as shown in Figure 5, that also in *N. cellanus* there is no correlation between the strength of the gumfoot bundles and their sizes. Due to the lack of data for other bundles, however, it is here hard to say if this could be due to a general lack of defect scaling in the silk products of this species. Finally, Table 4 and Figure 6 show once again the importance of considering the Young's modulus variations in natural silk bundles, as the p-values found for the $\sigma \propto \sqrt{E/d}$ are lower than the ones found for $\sigma \propto \sqrt{1/d}$ for all silk products excluded 4 fibres drop-down draglines, which are influenced by the small sample size.
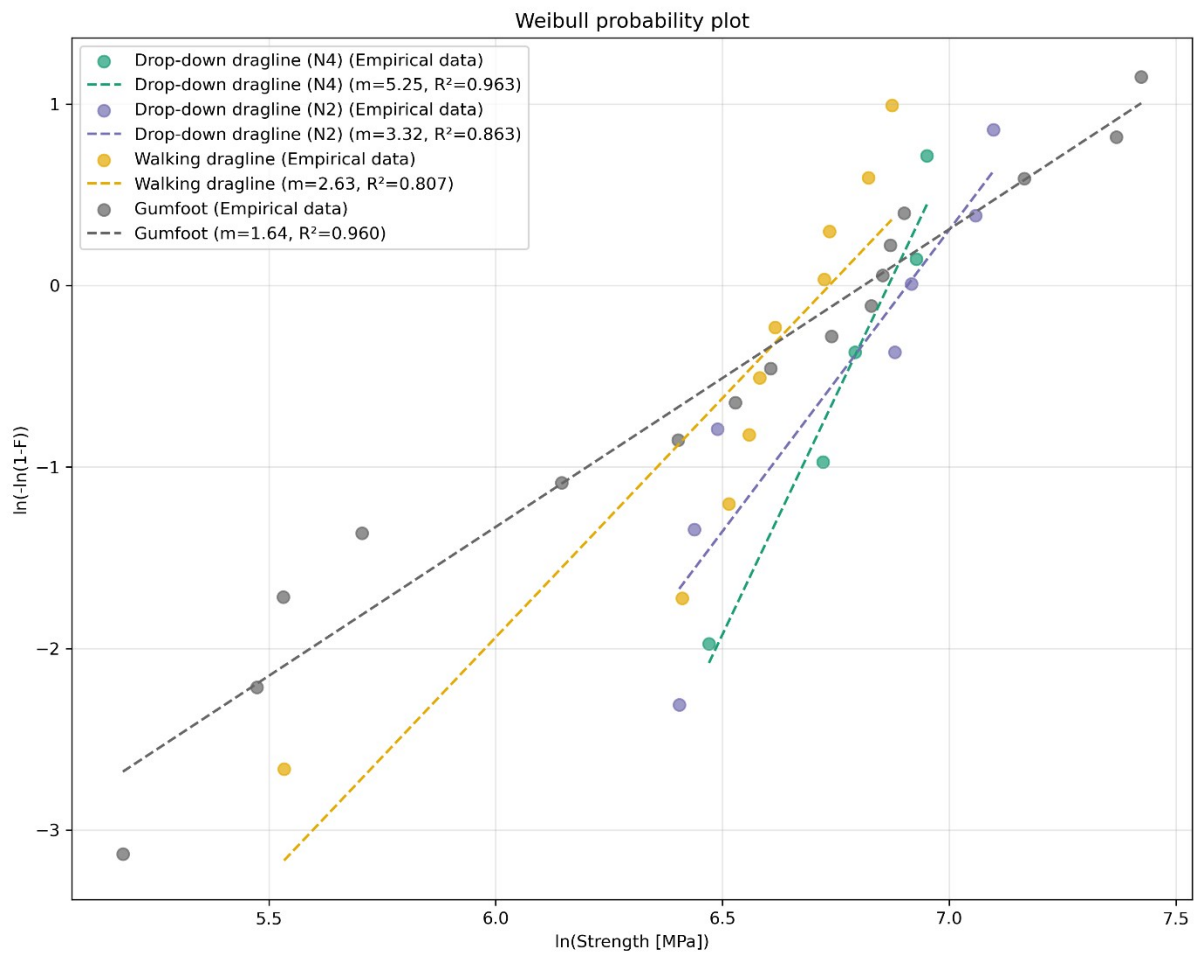

Figure S4 Weibull plot for *N. cellanus*, with linear regression results reported as dashed lines for each silk bundle type. All bundle types agree with the weakest-chain link distribution.
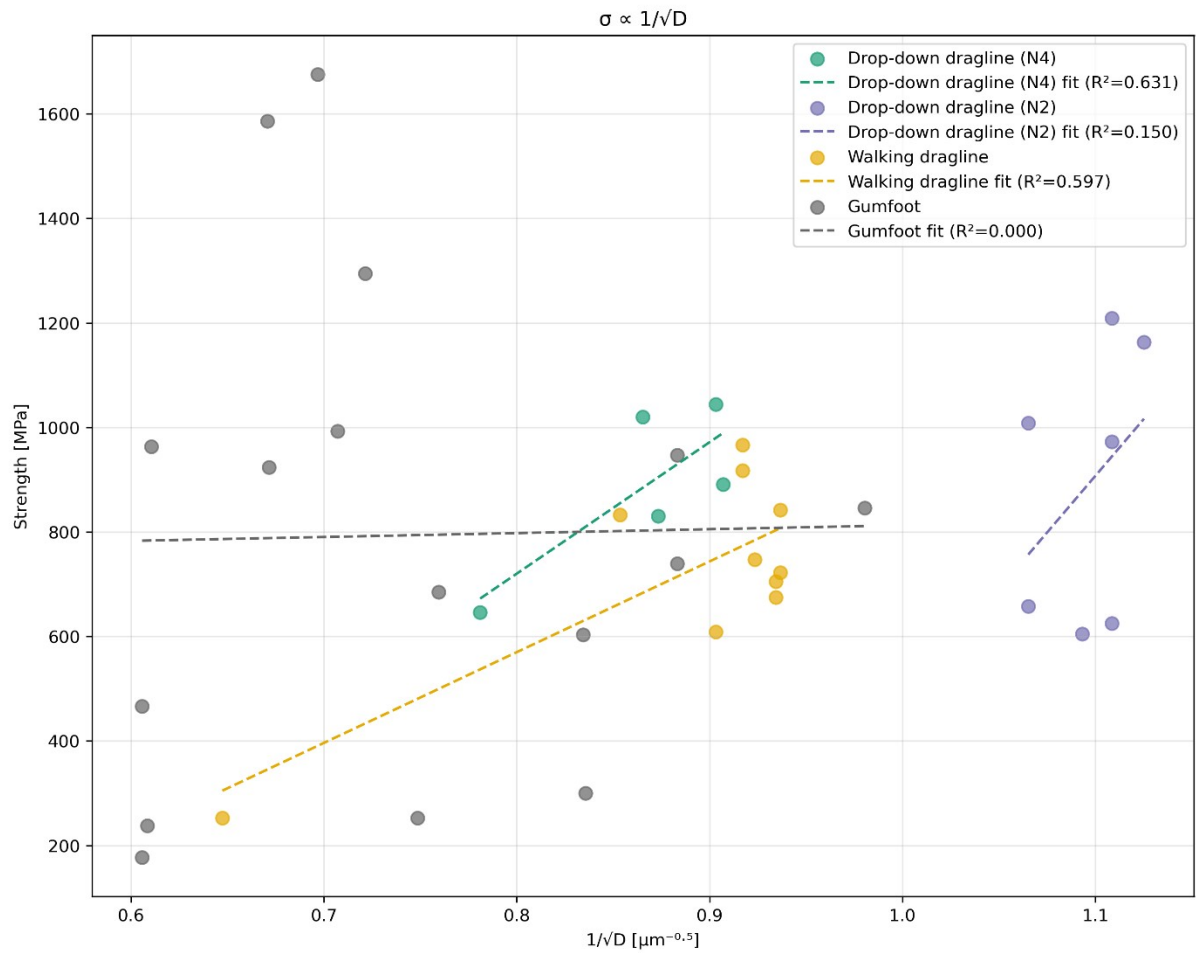
Figure S5 Fracture mechanics relationships for *N. cellanus* silk bundles, considering only the diameter as scaling parameter and ignoring the Young's modulus variation. Gumfoot bundles show no correlation between their size and their strength. Walking draglines and drop-down draglines all have similar diameters, affecting the goodness of the measurement. However, it is visible.
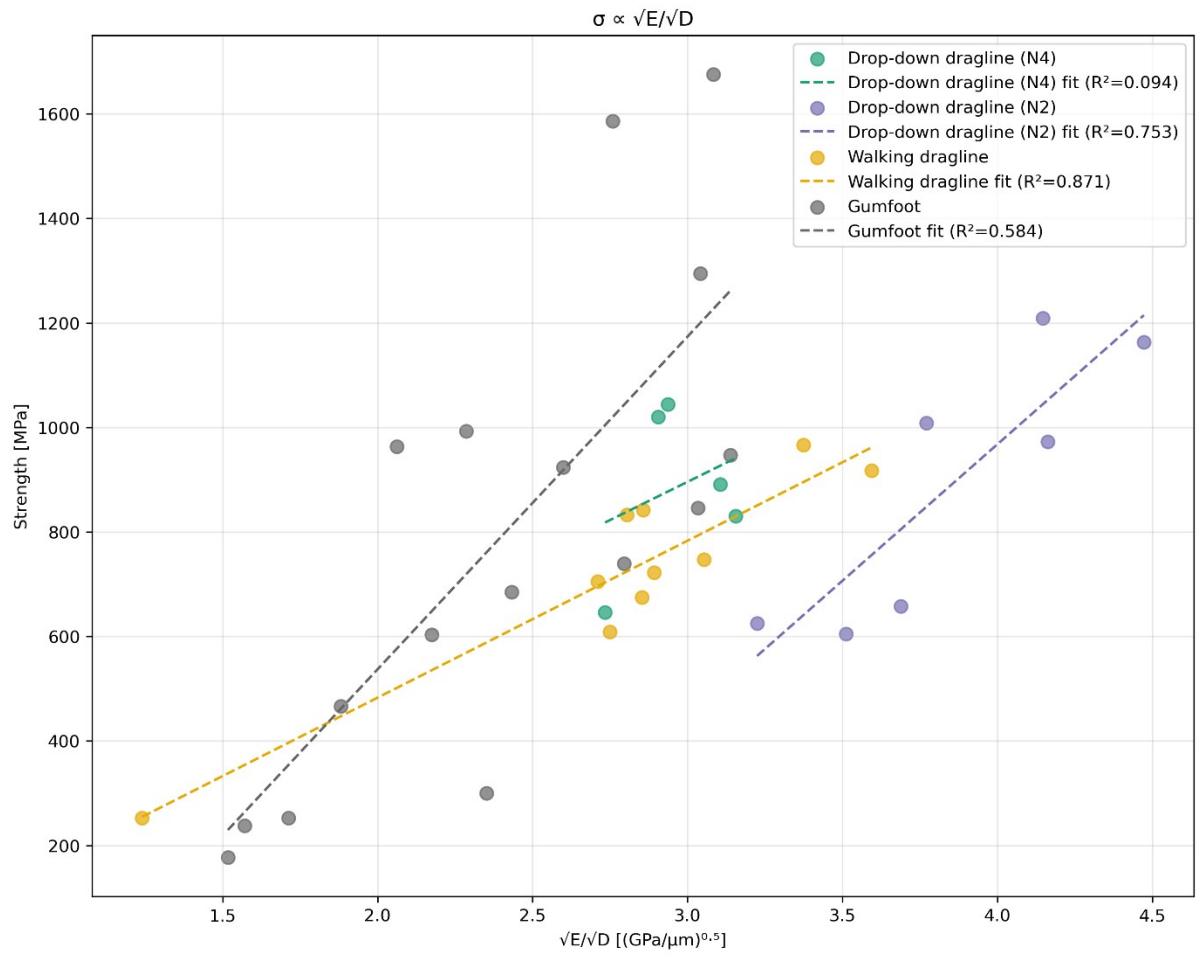
Figure S6 Fracture mechanics relationships for *N. cellanus* silk bundles. The plots demonstrate the correlation between stress at break and the square root of the modulus-to-diameter ratio for 2 fibres drop-down draglines and walking draglines. Sufficient data is missing to assess the proportionality for the 4-fibre drop-down draglines.

Table S3 Results of the two-parameter Weibull analysis conducted on each silk type for *N. cellanus*, and the scale parameter v found when studying the proportionality between strength and cross-section according to the modified Weibull distribution, with between brackets its significance.

Silk Type	Sample Size	σ [MPa]	$\Delta\sigma$ [MPa]	CV	m	σ_0 [MPa]	R^2	v
Drop-down dragline (N4)	5	886.3	144.1	0.163	5.25	959.2	0.963	3.509 (ns)
Drop-down dragline (N2)	7	891.6	239.9	0.269	3.32	1000.2	0.863	4.163 (ns)
Walking dragline	10	727	189.8	0.261	2.63	842.0	0.807	1.949 (**)
Gumfoot	16	793.3	443.8	0.559	1.64	907.9	0.96	0.333 (ns)

Table S4 Fracture mechanics analysis correlating bundle equivalent diameter with tensile strength for N. cellanus, using the relationships $\sigma \propto \sqrt{E}/\sqrt{d}$ and $\sigma \propto 1/\sqrt{d}$ for each silk bundle type, presenting coefficients of determination (r^2), statistical significance (p values).

Silk Type	d [μm]	E [GPa]	σ vs $\sqrt{E/d}$ p-value	σ vs $\sqrt{E/d}$ R^2	σ vs $\sqrt{1/d}$ p-value	σ vs $\sqrt{1/d}$ R^2
Drop-down dragline (N4)	1.35	11.77	0.6167	0.0936	0.1086	0.6306
Drop-down dragline (N2)	0.83	12.46	0.0114	0.7530	0.3899	0.1504
Walking dragline	1.31	10.01	0.0001	0.8708	0.0088	0.5968
Gumfoot	1.95	11.00	0.0006	0.5835	0.9449	0.0004

On the internal mechanical properties of silk bundles and their fibres

As shown in the last sections, one of the most important properties of the silk bundles is their variation of mechanical properties. Our SEM images confirmed that the bundles of *P. phalangioides* are composed of fibres running in parallel, fibres that can be found both in contact or distant from each other. The behaviour of fibres in parallel is a well-studied subject [14-18]. In its simplest theoretical implementation, the load carried by a bundle of fibre can be computed using Hooke's law: the force at each strain corresponds to the sum of the load carried by each fibre in the bundle for that value of strain, i.e. a bundle of parallel fibres has a stiffness equal to the sum of the stiffness composing it. This simple formulation is a consequence of the linear elastic model, and thus has to be applied carefully when dealing with high non-linear materials, as spider silk. Positive and negative interactions can arise from, to name a few: crossing interaction between fibres due to coiling[16, 17]; stress propagation from one fibre to the other after partial fracture of the fibres inside the bundle[15]; friction-driven interactions between the fibres [18]; the presence of hidden lengths inside the bundles [19, 20]. As a result, the strength and toughness of a bundle can be extremely different from the simple linear combination of the strengths and toughness of the fibres forming it. However, given specific experimental conditions, some assumptions still hold.

In our experiments, fibres are perfectly clamped at the two extremities and are pulled at a constant strain rate, by applying a displacement. A system of any number of clamped fibres in displacement control follows, in the linear region, Hooke's law [15]. This means that the stiffness of a bundle near the origin, i.e. the initial slope of the load-displacement curve, is indeed given by the linear combination of the fibres forming it. To confirm this, we implemented a Finite Element Method (FEM) to confirm that different contact scenarios between fibres do not affect the linear phase of bundles, using different geometries inspired by the SEM images we have collected (Figure 7). We used the linear solver MOFEM[21]. Table 5 presents the parameters used in this work, however these do not influence the results presented here, and any other set of parameters could be chosen. Our model revealed that the contact between the fibres does not affect the load carried by the bundle in the elastic region, as expected by a linear relationship and a uniform material: even when considering complete fusing between four fibres, the load measured it is coincident with the one measured when the fibres are separated from each other, and with the one calculated by applying Hooke's law. This indicates that, for small deformations and in a quasi-static experiment, it is possible to apply linear elasticity to fibre bundles of any geometry. This holds true even if changing the position, stiffnesses, and non-linear response of the fibre forming the bundle: all of these parameters affect the bundle only after partial fracture is observed, and thus mechanical properties change how stresses redistribute along the now non-uniform cross-sections along the bundle length. To study if this could partly explain our experimental results, we investigated partially fractured bundles using the FEM described before.

The FEM analysis confirmed that partial fracture of our bundles should lead to total failure of the bundle. The stresses accumulate at the interfaces of the broken fibre and the contact between different fibres, as shown in Figure 8. When considering realistic ranges for silk-based materials, the found stresses at the interface are high enough to lead to immediate crack propagation, and thus total bundle failure. This result is in agreement with the results shown in Table 1 and Table 2: the strengths follow a Weibull distribution, and the cross-sectional area and the young's modulus of each bundle correlates with the strength, indicating that the overall behaviour of the bundles is similar to the one that it would have if it was a single fibre of equivalent cross-section. Indeed, our load-elongation curves do not show

multiple prominent peaks: this indicates the absence of multiple, independent fractures happening in the bundle, while it is compatible with the presence of a single avalanche, which causes total failure of all the fibres for the same strain value[15].
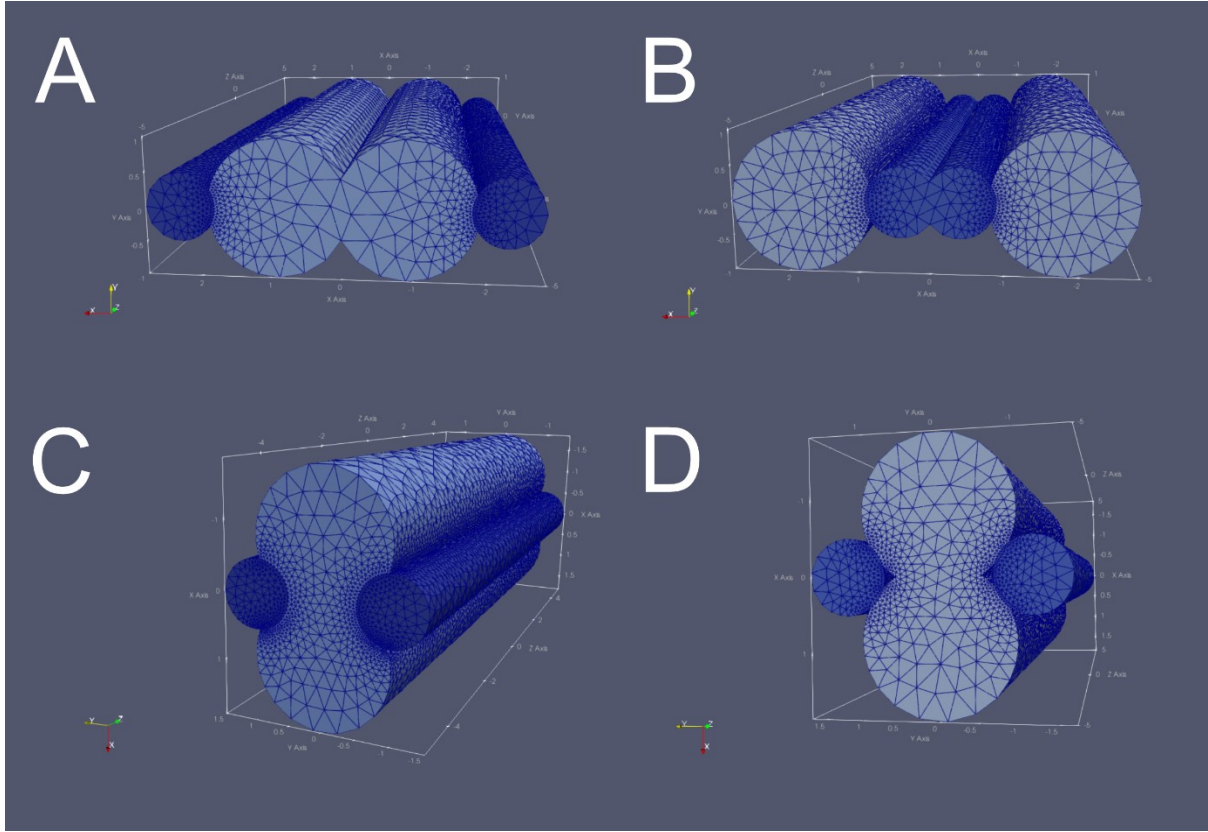

Figure S7 Four geometries used in our linear elastic Finite Element Method to verify stress distributions in the bundle during the elastic phase. Different Young's moduli can be assigned to different volume portions for each mesh.

Table S5 Overview of simulation parameters used in the FEM model. We note that the chosen parameters do not influence the results presented in this study.

| Symbol	Parameter	Value
ν	Poisson's ratio (both fibres)	0.3
L	Fibre length (both fibres)	10 μm
R_{small}	Fibre diameter (small fibres)	1 μm
R_{big}	Fibre diameter (big fibres)	2 μm
ε_{sim}	Simulated strain	0.1
$\sigma_{b, big}$	Stress at break (big fibres)	0.5 GPa
E_{big}	Young's modulus (big fibres)	2.5 GPa
$\varepsilon_{b, big}$	Strain at break (big fibres)	0.1 – 0.4
E_{small}	Young's modulus (small fibres)	0.1 GPa – 25 GPa
$\sigma_{b, small}$	Stress at break (small fibres)	0.1 GPa – 1 GPa
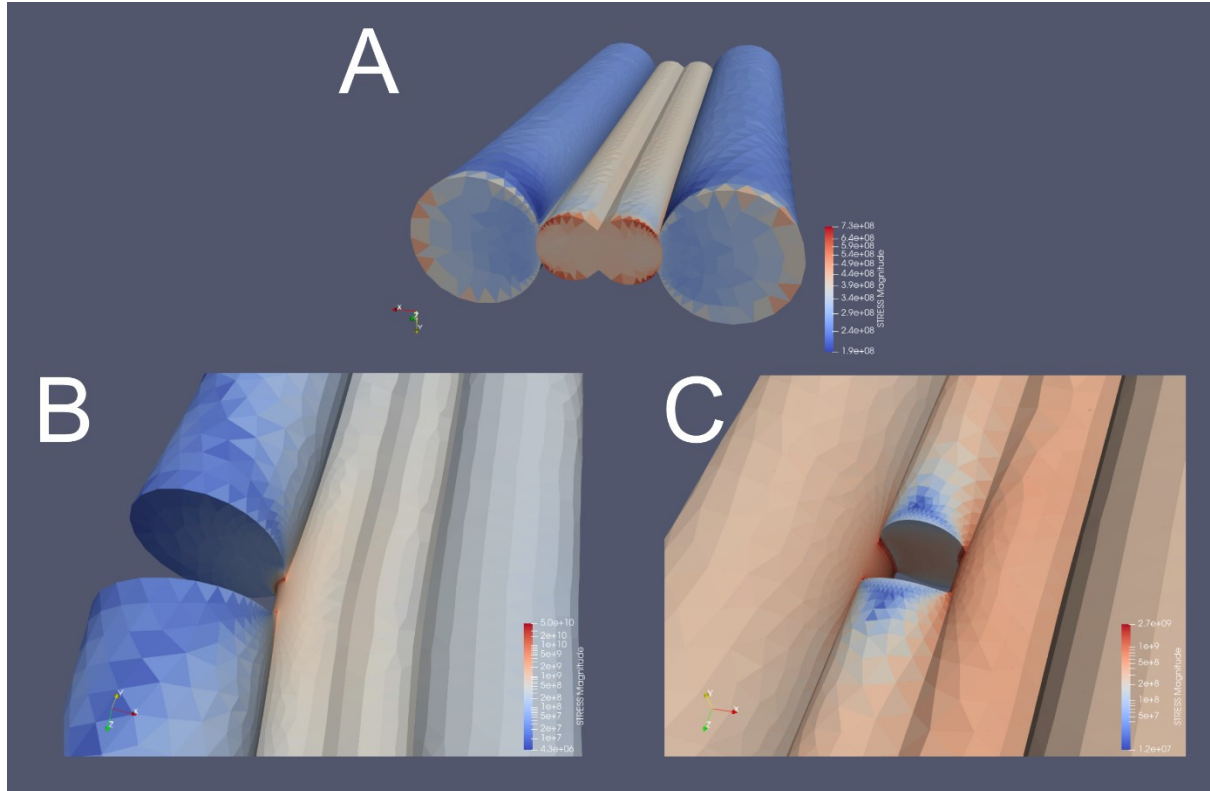
Figure S8 Stress distributions found for different geometries and partial fracture configuration. A) Intact bundle. For every intact bundle, the stress distribution found was homogeneous outside of the region where the fixed displacement was applied, and the ratio between the stresses in the different materials reflected the ratios between the different Young's moduli for every parameter combination. B) When a partial fracture is observed in one of the fibres, here a fibre of bigger diameter, stresses concentrate at the interface with neighbouring fibres for all contact scenarios. Stresses at the interface between the neighbouring fibre and the fracture are $\simeq 100$ times higher than in figure A. C) Identical scenario for a fracture happening on a smaller diameter fibre. Here, stress concentrations lead to stresses $\simeq 4$ higher than in Figure A. In both figures B) and C), stress concentration leads to an avalanche that leads to immediate fracture of the entire bundle.

Another phenomenon which is known to decrease the effective Young's modulus in the linear region is the presence of non-heterogeneous slacks inside the bundle, leading to fibres not participating to the stress load until a certain strain threshold [19, 20]. In our SEM images, and in our mechanical data, we have, however found no typical signs of these slacks, as a later rise of the slope of the load-displacement curve, or the presence of ribbons and other geometrical features in the bundle. Finally, the collection rate at which silk is produced is known to possibly affect the mechanical properties of silk: however, it was tested for *T. clavata* by Yazawa and Sasaki[22] that collection at different speed and humidity conditions did not have a significant impact on the Young's modulus.

The practical consequence of this conclusion, is that we expect the Young's modulus of bundles based on single fibre types to be lower than heterogeneous fibre bundles. This behaviour is observed in our data regarding *N. cellulanus*: dropdown draglines made of 2 and 4 fibres have a relative standard deviation of 19.93% (N = 7) and 8.02% (N = 5), respectively. These values are compatible with the range of relative standard deviations found in literature for single major ampullate fibres of Araneidae [22–24]. The relative standard deviations we found for heterogeneous bundles is higher, with a value of 37.91% for gumfoot silk bundles (N = 17) and 31.04% for walking draglines (N = 10).

Our results for *P. phalangioides* reveal however a richer variety of moduli. Bridging lines are produced by this spider species using only minor ampullate silk: however, the aggregated data shows a relative standard deviation of 41.77% (N=17). The same is true for manually collected aciniform silk: however, its relative standard deviation 52.79% (N=10) is affected by the low value of its Young's modulus. Dropdown draglines silk threads, a bundle known to be composed by two major ampullate silk threads, show a standard deviation of 27.18% (N=12).

We have also considered the slope of the curve in the load-strain curve, without dividing it by the measured cross-section (or, in other words, we multiply the Young's modulus by the cross sectional area for each bundle). This value, is usually a bad reference to identify the material type, as it does not consider the possible geometric variations of silk. The relative standard deviation values for this parameter are indeed twice as high for gumfoot bundles of *N. cellulanus* than what is found for the related Young's modulus; however, for *P. phalangioides*, the dropdown dragline silk shows a relative standard deviation of 19.65% for 2 fibre draglines and 13.71% for 4 fibre draglines. When focusing on single individuals, the results about the stiffnesses of the bundles become even more revealing: 2 fibres dropdown draglines shows an average relative standard deviations across specimens of 15.40% (N=4); walking draglines shows an average relative standard deviations across specimen of 8.72% (N=5); bridging lines show an average relative standard deviation across specimen of 23.20%, a result particularly meaningful when compared to the 33.59% value obtained when considering all stiffness values together, independently from the specimen, or all the Young's moduli, 41.77%. In practice, this indicates that the silk properties of these bundles show a higher consistency before normalisation, and when considering each individual independently, as if each spider he's able to produce materials and bundles capable to reach a certain force rather than a certain stress. This also explains the importance of the young's modulus in the strength scaling predicted by the Griffith criterion presented in Equation (4) and discussed in the previous section. This extreme variability and adaptability of the silk mechanical properties could be an advantage for a cosmopolitan spider as *P. phalangioides*.

Due to the extreme variability of silk properties of single fibres and fibre bundles, it is unfeasible to try to derive the composition of the bundles of *P. phalangioides* starting from the biological and mechanical constraints known. In particular, bundles containing both major and minor ampullate silk do not show any significant difference between their behaviour; this is complicated by the fact that bridging lines, known to be made only from minor ampullate silk, show a Young's modulus compatible with the dragline bundles, independently from their number of fibres. The results presented in this work suggest that we should reconsider how we historically gathered data regarding the mechanical properties of spider silk, as for *P. phalangioides*, and potentially other spiders, the average values of the mechanical properties of their dropdown draglines does not capture the observed complexity. Future studies should focus on the internal composition and mechanics of these extremely variable bundles. Moreover, we highlight the importance of considering naturally produced silk in similar studies. This study suggests that spinning conditions and spider behaviour could have a higher effect on spider silk properties than what is currently considered in the literature.

On the consequence of a lack of interaction between fibres in clamped bundles under uniaxial tension

Our study shows that *P. phalangioides* silk bundles can include major ampullate fibres, minor ampullate and aciniform fibres. In this study, we also discuss how the empirical, numerical and statistical analysis all validate the assumption that the fibres included in these bundles are in strong contact, and how this affects the behaviour of the bundle after first fracture, but not before so. To clarify this concept, we here show a numerical solution of the Fibre Bundle Model (FBM) applied to a six fibre bundle[15] . We note here, that for a stiffly clamped system of fibres, non-interacting between themselves, and for a low number of fibres with discernible properties (i.e., that do not need to be represented as a distribution function), the FBM reduces itself to a simple problem of non-linear fibres in parallel under externally applied monotonously increased strain. The properties of each fibre type are shown in table. The critical strain is assumed to be normally distributed across a mean value, with a width of the distribution equal to 10% of the mean critical strain value. As the fibres are assumed to be non-interacting and under monotonous stretch, we could also consider non-linear behaviours[20] although that wouldn't change qualitatively the result shown here. We report here one exemplary result in Figure S6. We can see from the theoretical predicted curve that a failure of a large, load-bearing fibre, should lead to a distinct peak in the load-displacement curve. Each fibre fails independently, releasing its elastic energy to the infinitely stiff boundary condition. This result is independent from the specific properties assumed for the fibres. This is not what we observe in the empirical curves of our bundles, where the curve has a very smooth (draglines, bridging lines) or smooth (gumfoot) shape. According to the FBM, if a bundle is made of two identical fibres, differing only for their critical strain value, the load measures at that point would perfectly halve. This is in deep contrast with what we observe in our empirical results, where curves proceed in a smooth way, except for some small peaks observed in the curves of gumfoot threads. Moreover, we never observe surviving aciniform fibres, despite their nominal large critical strain, which should frequently surpass 40%.

The FBM explains that[2] load distribution could also be mediated by the presence of a soft clamping mechanisms able to transmit forces between the fibres through the edges, similar to what happens in a fibre reinforced composite with perfectly aligned fibres[2]. The theoretical investigation of this topic goes beyond the scope of this study: however, we have seen no evidence, in all of our tests on natural and artificial fibres, of such mechanism being present while using our tensile test machine. Furthermore, when testing artificial fibres or spider bundles of different spider species[20], we were able to discern perfectly the forementioned peaks in the load-elongation curve, in accordance to what predicted by the FBM.

Table S6 Parameters for FBM model simulation for the theoretical behaviour of a non-interacting bundle of three pairs of fibres with distinct mechanical and geometrical properties.

Fibre type	Number of Fibres	Diameter (μm)	Strength (GPa)	Mean critical strain
I	2	0.4	0.99	0.19
II	2	0.3	0.2	0.5
III	2	0.89	0.5	0.4
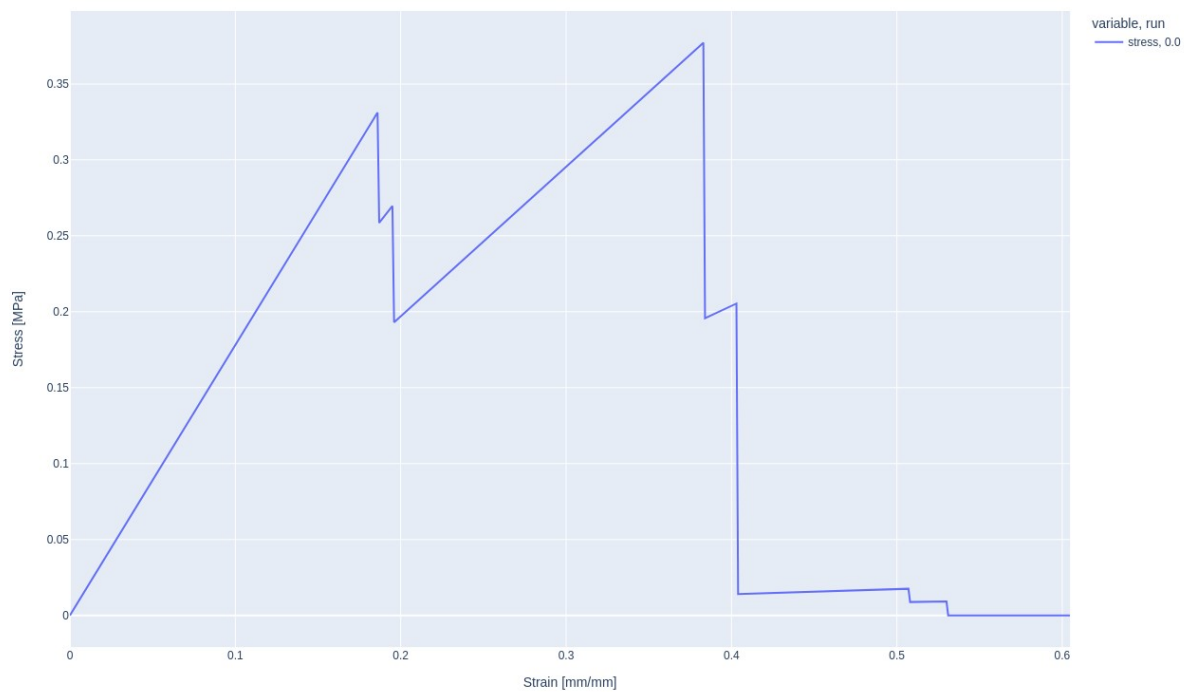
Figure S9 Theoretical quasi-static stress-strain curves of the expected mechanical behaviour of a bundle of three pairs of non-interacting fibres with different properties.

Method

Artificial fibre bundle preparation and testing

Nylon 6,6 fibre bundles (length 1 m, filament diameter 0.01 mm, 14 filaments, tex number 1.3) and low-density polyethylene (LDPE) fibre bundles (length 1 m, filament diameter 0.044 mm, 90 filaments, tex number 110) were purchased from Goodfellow Advanced Materials (Huntingdon, Cambridgeshire, UK.). Individual nylon and LDPE fibres were carefully separated from the bundles and recombined to create mixed fibre configurations. The fibres were mounted on 11 mm × 11 mm square-punched black cardboard frames lined with double-sided adhesive tape. Four fibre configurations were tested: single Nylon 6,6 fibre, single LDPE fibre, one Nylon–one LDPE bundle, and a bundle consisting of three Nylon 6,6 fibres and one LDPE fibre. Tensile tests were performed using a T150 Universal Testing Machine (KLA, Milpitas, California, USA) to record force–extension data. Tests were conducted at a constant extension rate corresponding to 1% strain per second until failure, with a load resolution of 50 mN and an extension resolution of 35 nm. For each configuration, five independent samples (N = 5) were tested.

From Figure S10, the stress–strain curves show that the Nylon 6,6 fibre exhibits much higher tensile strength compared to the LDPE fibre, which displays softer and more ductile behaviour. When the two materials were combined and tested together, the resulting stress–strain curve showed a distinct stress drop at around 35% strain, corresponding to the failure of the Nylon 6,6 fibre. In contrast, the LDPE fibre exhibited a strain at break of approximately 110%. Increasing the proportion of Nylon 6,6 in the bundle (Nylon6,6–LDPE [3:1] configuration) resulted in a higher stress at break compared to the Nylon6,6–LDPE [1:1] configuration, although the strain at break remained similar between the two configurations.
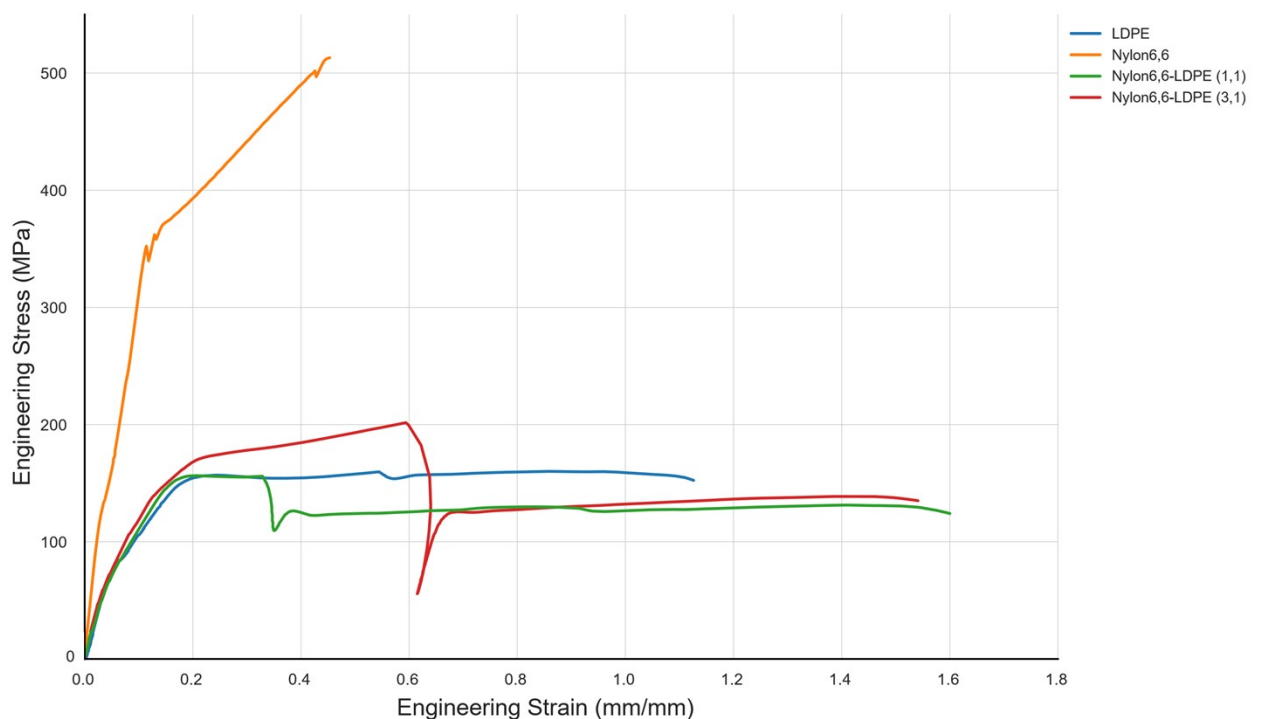
Figure S10 Exemplary stress–strain curves of individual LDPE (blue line) and Nylon 6,6 (yellow line) fibres, and of mixed bundles composed of Nylon 6,6 and LDPE fibres (green and red lines). The first bundle includes one Nylon 6,6 and one LDPE fibre (green line), while the second bundle contains three Nylon 6,6 fibres and one LDPE fibre (red line).
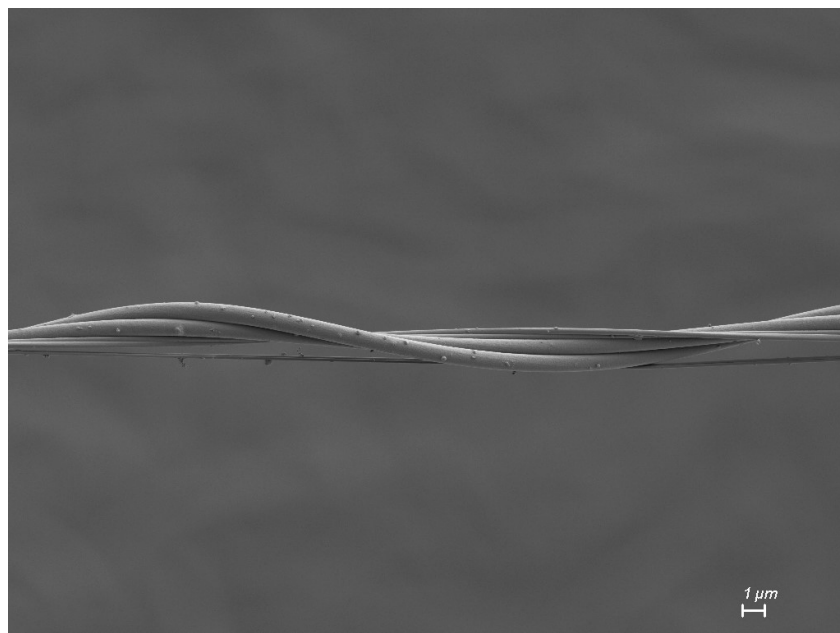

Figure S11 Morphology of a gumfoot thread illustrating areas where the individual silk fibres are not properly aligned or in full contact, forming loop-like or separated regions within the bundle structure.

Table S7. Sample sizes for each silk thread type from *Pholcus phalangioides* and *Nesticus cellulanus* used in mechanical property analyses.

Species	Silk type	Number of spiders	Number of samples
Pholcus phalangioides	Drop-down draglines (N2)	7	12
	Drop-down draglines (N4)	9	11
	Walking dragline	5	16
	Bridging line	8	17
	Gumfoot thread	6	14
	PMS (forcibly silked)	4	11
	Aciniform (forcibly silked)	5	10
Nesticus cellulanus	Drop-down draglines (N2)	2	7
	Drop-down draglines (N4)	2	5
	Walking dragline	2	10
	Gumfoot thread	4	10

(A)

200 nm

(B)

200 nm
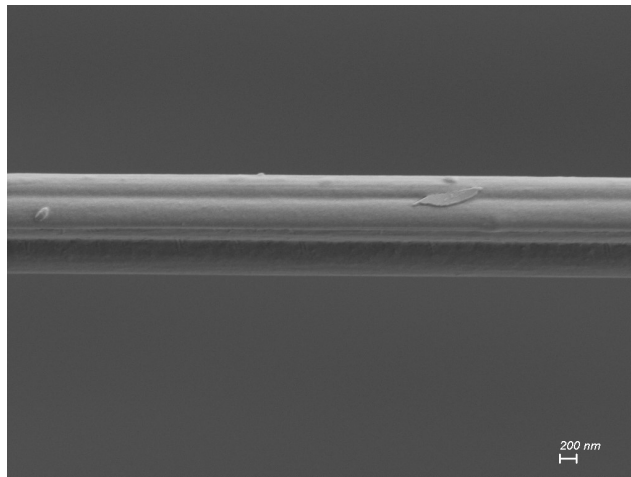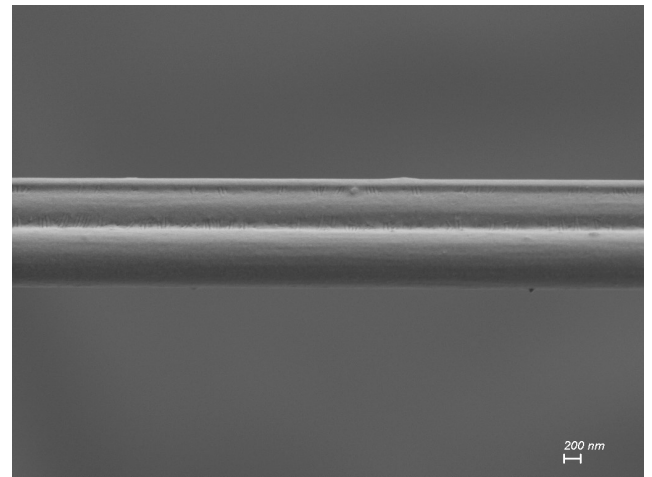
Figure S12 Scanning electron micrographs of N4 dragline samples stretched to 0.1 mm/mm strain. (A) Sample showing a thin surface coating that caused several fibres to adhere closely to one another. (B) Sample displaying shallow scratch-like surface features between adjacent fibres. These patterns are interpreted as local surface artefacts rather than mechanically induced deformation.
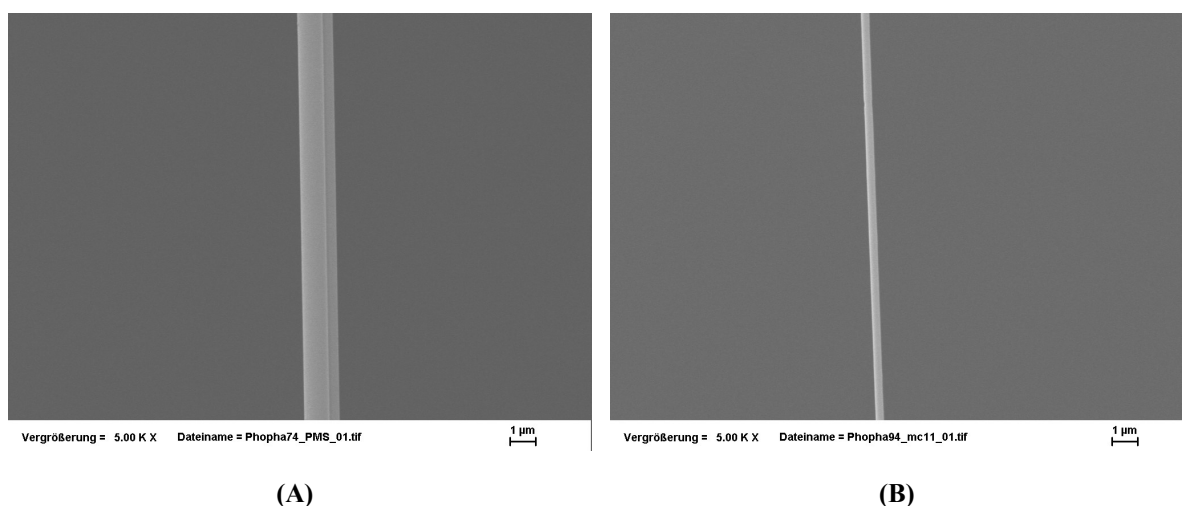
Figure S13 Scanning electron micrographs of forcibly spun (A) posterior median spinneret (PMS) thread and (B) aciniform fibres from Pholcus phalangioides. These images are provided for comparison only, as forcibly spun fibres do not reflect natural spinning conditions.

References

1.   W. Weibull, *Journal*, 1939.
2.   A. Hansen, *Frontiers in Physics*, 2020, **Volume 8 - 2020**.
3.   T. S. Creasy, *Composites Science and Technology*, 2000, **60**, 825-832.
4.   E. Trujillo, M. Moesen, L. Osorio, A. W. Van Vuure, J. Ivens and I. Verpoest, *Composites Part A: Applied Science and Manufacturing*, 2014, **61**, 115-125.
5.   K. Naito, *Journal of Applied Polymer Science*, 2013, **128**, 1185-1192.
6.   A. S. Watson and R. L. Smith, *Journal of Materials Science*, 1985, **20**, 3260-3270.
7.   G. Greco and N. M. Pugno, *Molecules*, 2020, **25**, 2938.
8.   F. Wang and J. Shao, *Polymers*, 2014, **6**, 3005-3018.
9.   Z. P. Xia, J. Y. Yu, L. D. Cheng, L. F. Liu and W. M. Wang, *Composites Part A: Applied Science and Manufacturing*, 2009, **40**, 54-59.
10.   S. Kochiyama, *Non-classical scaling of strength with size in marine biological fibers*, 2024.
11.   A. A. Griffith, *Philosophical Transactions of the Royal Society of London. Series A, Containing Papers of a Mathematical or Physical Character*, 1921, **221**, 163-198.
12.   G. R. Irwin, *Journal of Applied Mechanics*, 2021, **24**, 361-364.
13.   D. Porter, J. Guan and F. Vollrath, *Adv Mater*, 2013, **25**, 1275-1279.
14.   F. Kun, in *Creep and Fatigue in Polymer Matrix Composites*, ed. R. M. Guedes, Woodhead Publishing, 2011, pp. 327-349.
15.   P. C. H. a. S. P. Alex Hansen, *The Fiber Bundle Model*, Wiley, 2015.
16.   M. Fraldi, G. Perrella, M. Ciervo, F. Bosia and N. M. Pugno, *Journal of the Mechanics and Physics of Solids*, 2017, **106**, 338-352.
17.   A. Cutolo, A. R. Carotenuto, S. Palumbo, F. Bosia, N. M. Pugno and M. Fraldi, *International Journal of Mechanical Sciences*, 2021, **192**, 106135.
18.   Z. Halász, I. Kállai and F. Kun, *Frontiers in Physics*, 2021, **9**, 613493.
19.   S. R. Koebley, F. Vollrath and H. C. Schniepp, *Materials Horizons*, 2017, **4**, 377-382.
20.   D. Liprandi, M. Ramírez, S. Schlüter, L. Baumgart, A. C. Joel, et al., *Interface Focus*, 2024, **14**, 20230071.
21.   L. Kaczmarczyk, Z. Ullah, K. Lewandowski, X. Meng, X. Zhou, et al., *Journal of Open Source Software*, 2020, **5**, 1441.

22. K. Yazawa and U. Sasaki, *International Journal of Biological Macromolecules*, 2021, **168**, 550-557.